PCCP

Accepted Manuscript

ROYAL SOCIETY OF CHEMISTRY

www.rsc.org/pccp

Journal Name

RSCPublishing

ARTICLE

Carbon nanotubes enhanced Seebeck coefficient and power factor of rutile TiO_2

Cite this: DOI: 10.1039/xoxxoooooox

Yao-Cheng Lai[a], Hsin-Jung Tsai[a], Chia-I Hung[a], Hiroyuki Fujishiro[b], Tomoyuki Naito[b], and Wen-Kuang Hsu[a,*],

Received ooth January 2012,
Accepted ooth January 2012

DOI: 10.1039/xoxxoooooox

www.rsc.org/

Seebeck coefficient, according to Ioffe's approximation, is inversely proportional to carrier density and decreases with doping. Here we find that incorporation of multi-walled carbon nanotubes into rutile TiO_2 improves electrical conductivity and Seebeck coefficient at low filling fraction of tubes; the former is owing to lengthening of mean free path and doping modified carrier mobility for the latter. Tube-oxide mixing also causes significant phonon drag at interfaces and reduced thermal conductivity is verified by promoted figure of merit.

Introduction

Materials that show potential in thermoelectric powering (TEP) have drawn much attention in recent years. Three factors determine efficiency of energy conversion at a given temperature (T) and can be linked through a dimensionless parameter known as figure of merit $ZT = \sigma S^2 T/k$, where σ is electrical conductivity, S is Seebeck coefficient, σS^2 is power factor and k is thermal conductivity[1]. Scattering plays a crucial role in determining σS^2 and has been verified by alloying Bi with Sb and Te[2,3]. Study reveals that alloying creates multi-domains and carriers encounter a Schottky-like barrier at interfaces[3]. In this case, interfacial scattering occurs and reduced k leads to ZT promotion[3]. Cited alloys however are toxic in nature and produce environmental issue. Accordingly, seeking of replacements becomes important and study currently focuses on oxides, including ZnO, $CaMnO_3$, $NaCo_2O_4$, $Ca_3Co_4O_9$, $In_2O_3{\cdot}SnO_2$ and TiO[4-7].

Oxides, however, lack of free carriers and large σS^2 only emerges at high T, e.g. $In_2O_3{\cdot}SnO_2$ gives $\sigma S^2 = 1.6\times10^{-4}$ $Wm^{-1}K^{-2}$ at T = 1300 K[4]. Doping may promote carrier density (n)[8] to some extent and has been carried out on $CaMnO_3$ using Bi as dopants[5-7]. ZT however does not significantly increase with doping and underlying mechanism has been interpreted according to the Ioffe's approximation

$$S = \pm\frac{k_B}{e}\left[r + 2 + ln\frac{2(2\pi m^* k_B T)^{3/2}}{h^3 n}\right]$$

where k_B is Boltzmann constant, e electron charge, r is absolute scattering factor, m^* is effective mass and h denotes Planck's constant[8]. Equation clearly indicates that S is inversely proportional to n (i.e. $S \propto n^{-1}$) and σ is improved at the expense of S. TiO_2 is eco-friendly and its photo-catalytic character has been proved capable of promoting charge storage in solar cell as well as supercapacitor[9]. He *et al* have studied the TiO_x at T = 20°C and found a positive S at x = 1.2-1.7. S then transits into negative at x = 1.7 and reaches the maximum at x = 2[10]. Again, TiO_2 shows a low σS^2 and ZT lies on 0.1-0.2 at T = 700-1100 K[10,11]. In this work, multi-walled carbon nanotubes (MWCNTs) are thermally mixed with rutile TiO_2 and resultant composites exhibit increased σ and reduced k at a low filling fraction of tube (f_{CNT}), i.e. amplified σ/k. Both k and σ significantly increase as f_{CNT} approximates electrical percolation threshold (τ) and improvement is owing to tube networking. Surprisingly, S is also promoted and displays $S \propto f_{CNT}$ prior to τ. S then decreases and approaches the positive regime at $f_{CNT} \sim \tau$, indicative of p-type CNTs governed TEP. Study here shows TEP improvement by 5553% for σS^2 and 7380 % for ZT at T = 300-523K.

Experimental

Synthesis

MWCNTs (95% purity, Legend Star International Co., Ltd) and TiO_2 (P25, average particle size ~25nm, Aldrich) are dispersed in ethanol using a planet ball milling (290 rpm, ball size = 3 mm and 4 h). Dispersion is then dried at 60°C and remaining solid mixture is sintered by spark plasma sintering (SPS) technique at 1200 K; the CNT content in oxide being 0.1 wt% ($TC_{0.1}$), 0.5 wt% ($TC_{0.5}$), 1 wt% (TC_1), and 10 wt% (TC_{10}) respectively.

Materials Characterization

Composite texture is inspected by scan electron microscopy (SEM) and the bonding characters are analysed using raman and X-ray photoelectron spectroscopy (XPS). A four-wire technique is employed to probe σ and S at 300-523 K; the former is carried out using a Keithley-4200 power supply with background noise controlled at ± 0.5 nA. The k is determined according to equation $k = \varphi C_p \rho$, where ρ is material density, C_p is heat capacity and φ is thermal diffusivity. First, samples are pressed into pellets and are sandwiched between thin carbon

films as reference. Second, φ and C_p are probed by the laser-flash technique (LFA-447) and differential scanning calorimetry (DSC) at 10°C/min.

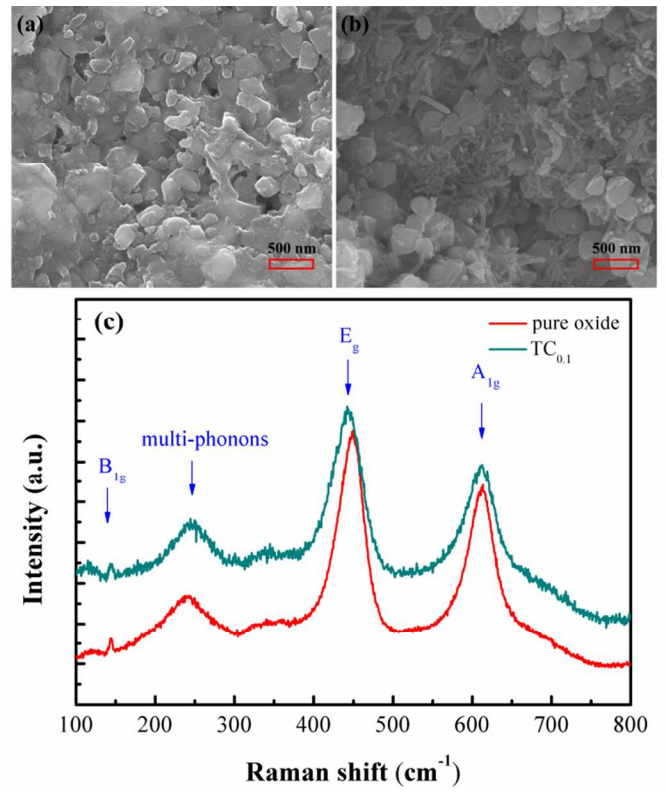

Fig. 1. SEM images of pure oxide (a) and $TC_{0.1}$ (b) and corresponding Raman spectra (c).

Band structure, including energy gap (E_g) and LUMO/HOMO states at E_F, is calculated using *ab-initio* method (CASTEP) as follows. First, an extended oxide structure is built in a 2×2×2 superlattice and is geometrically optimized with the generalized gradient approximation (GGA). Second, the ultrasoft pseudopotential and Monkhost-Pack grid are set at 480 eV and 0.05Å^{-1}. Third, the m^* at the minimum of LUMO and maximum of HOMO is determined according to equation below.

$$\frac{1}{m^*} = \frac{1}{\hbar^2}\frac{\partial^2 \mathrm{E}(k)}{\partial k^2}$$

where $\hbar$ and k are reduced planck constant and wave-vector and, the E(k) denotes energy with respect to k[12]. Similar procedures are also applied to carbon doped oxide structure with doping content of 0.1wt%. For the sake of accuracy, E_g is also measured by diffuse-reflectance uv-vis spectroscopy and obtained data is fit with equation $\alpha h\nu = C(h\nu - E_g)^{\gamma}$ where α is linear absorption coefficient, ν is incident frequency, C is proportionality constant and γ is a constant determined by E_g, i.e. γ = 0.5 for direct E_g and γ = 2 for indirect E_g [13-15].

Results and discussion

Sintering causes fusion and oxide particles become interconnected (Fig. 1(a)). Addition of CNTs into oxide creates low resistance paths and joule heating takes place mainly at

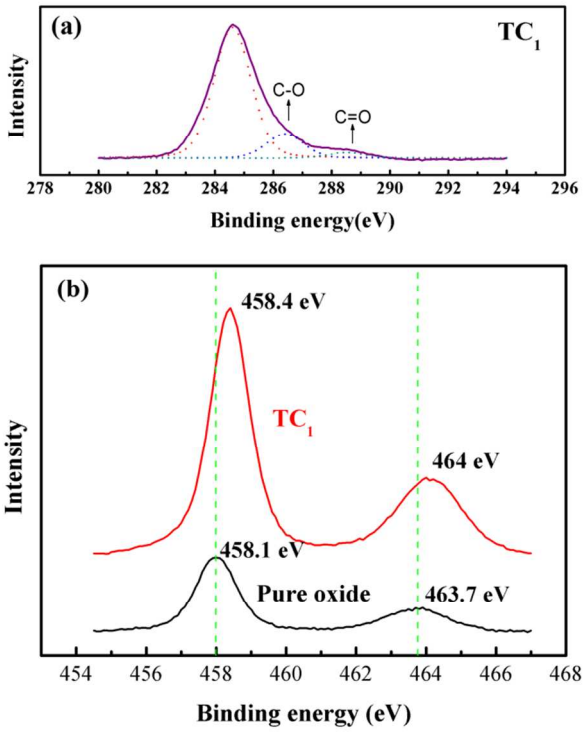

Fig. 2. XPS spectra of TC_1 at 280-294 eV (a) in comparison with oxide at 454-468 eV (b).

embedded tubes. Accordingly, oxides remain granulated and are decorated with dispersed tubes (Fig. 1(b)). Fig. 1(c) displays raman spectra of sintered oxide (red) in comparison with $TC_{0.1}$ (green). For rutile phase, the Raman-active modes due to site symmetry appear at 143 cm^{-1} (B_{1g}), 447 cm^{-1} (E_g) and 612 cm^{-1} (A_{1g}), along with a broad feature arising from multi-phonon processes at 235 cm^{-1} (red)[16-18]. The E_g mode becomes shifted (~9 cm^{-1}, green) as tubes are added and phenomenon may come from carbon doping. First, XPS spectra exhibit C1s peak at 284.6 eV and distinguishable features at 286.4 eV and 288.5 eV correspond to C-O and C=O bonds (Fig. 2(a))[19]. Second, the E_g mode is nonpolar in nature and mode frequency is essentially determined by bond length and strength[17]. In other words, Ti is replaced by C and carboxyl forms. Third, carbide (TiC) is absent in XPS spectra, excluding O-C substitution. Fourth, doping induces blue-shift in Ti^{4+} spectra and peaks move by 0.25 eV for $Ti2p_{1/2}$ (463.7 eV) and 0.3 eV for $Ti2p_{3/2}$ (458.1 eV) (Fig. 2(b))[19,20]. Fifth, Ti-C substitution creates stresses (circle, Fig. 3. (a)-(b)) and charges redistribute (Fig. 3 (c)-(d)).

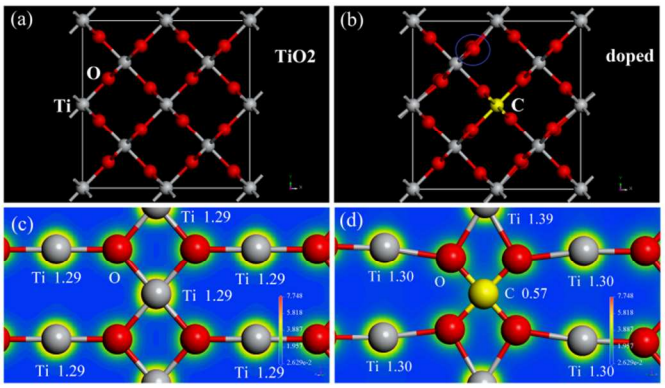

Fig. 3. The *ab-initio* simulated structure of pure oxide (a) and carbon doped oxide (b) and corresponding Mulliken charge dispersion of oxide (c) and doped oxide (d).

Fig. 4(a) displays σ profiles of pure oxide (red), $TC_{0.1}$ (blue), $TC_{0.5}$ (green), TC_1 (pink) and TC_{10} (yellow) at 300-523K. We find that improvement reaches one order of magnitude for $TC_{0.1}$, $TC_{0.5}$ and TC_1 and $\sigma \propto T$ is attributable to Boltzmann energy (k_BT) created carriers in CNTs[21]. For TC_{10}, σ increases by two orders of magnitude relative to oxide alone, confirming $\tau \sim f_{CNT}$ = 10 wt%. Two factors contribute to σ enhancement according to equation $\sigma = ne^2\eta/m^*$ where η is mean free path controlled relaxation time. Apparently, the η prevails and n increase due to carbon doping is limited. First, pure oxide has an E_g of 3.03 eV at Γ point and doping created n-type state lies at 2.674 eV (Fig. 4(b)). At 300K, the k_BT (= 0.0259 eV) is too low to create thermal carriers through band-to-band transitions, including valence band→doped state ($\Delta E_{v\text{-}d}$ =2.674 eV), doped state→ conduction band ($\Delta E_{d\text{-}c}$ = 0.356 eV) and valence band→ conduction band ($\Delta E_{v\text{-}c}$ = 3.03 eV) (Fig. 4(b)). Second, the sequence of $k_BT << \Delta E_{d\text{-}c} < \Delta E_{v\text{-}d} < \Delta E_{v\text{-}c}$ remains at 523K (k_BT_{523K} = 0.045 eV), indicative of unchanged n. Third, the uv-vis spectra support calculation and E_g is found to be 2.89 eV for oxide, 2.48 eV for $TC_{0.1}$, 2.41 eV for $TC_{0.5}$, 2.28 eV for TC_1 and 1.67 eV for TC_{10}, exceeding k_BT at 300K and 523K (Table 1 & Fig. 5(a)). Fourth, S is promoted from 470 μVK^{-1} (oxide) to 550 μVK^{-1} ($TC_{0.1\sim1}$) at 300K and from 500 μVK^{-1} to 610 μVK^{-1} at 523K, in contradiction with $S \propto n^{-1}$ (Fig. 5(b)). S then significantly decreases and approaches the positive regime at TC_{10}, again supporting p-type CNTs governed TEP (yellow, Fig. 5(b)).

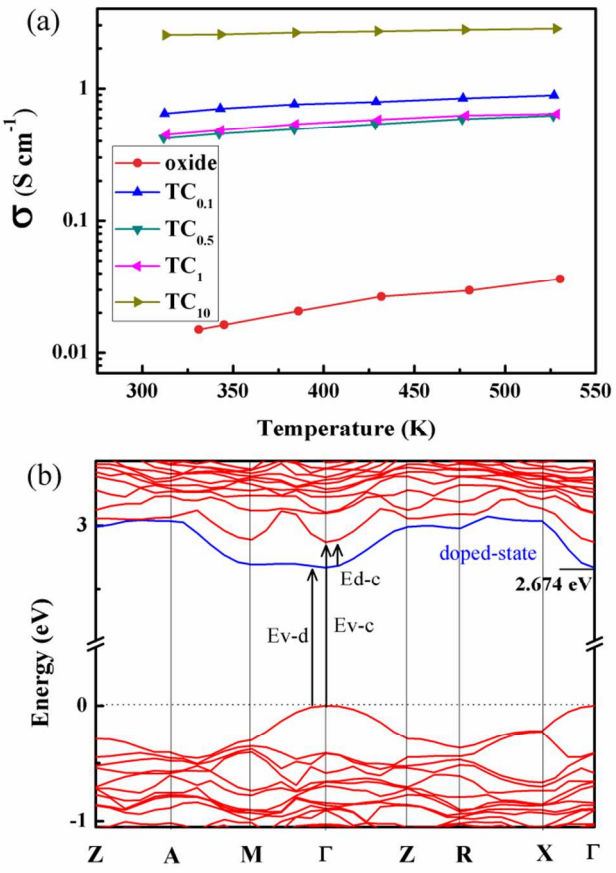

Fig. 4. The σ profiles of oxide and doped oxide at elevated T (a) and simulated band profile of doped oxide (b).

Table 1. E_g at various f_{CNT} in comparison with pure oxide.

Samples	oxide	$TC_{0.1}$	$TC_{0.5}$	TC_1	TC_{10}
Eg (eV)	2.89	2.48	2.41	2.28	1.67

CNTs conduct heat and are often dispersed in polymers to improve k. Incorporation of CNTs into a polymer, however, induces heat resistance at interfaces and effective thermal conduction appears to rely on tube-polymer cohesion[13]. The oxide-tube coupling, according to SEM inspections (Fig. 1(a)-(b)), is weak and enhanced scattering at interfaces is expected[13]. Measurements carried out at 300K yield k = 3.05 $Wm^{-1}K^{-1}$ for oxide and 2.2-2.39 $Wm^{-1}K^{-1}$ for $TC_{0.1\sim1}$, supporting enhanced scattering at tube/oxide contacts (Fig. 6(a)). Conduction paths are then switched from bulk oxide to tubes at $f_{CNT} \sim \tau$ and conversion is supported by (i) significant k increase and (ii) Umklapp process induced $k \propto T^{-1}$ in CNTs[22]; the latter being measured to be 3.02 $Wm^{-1}K^{-1}$ at 300K and 2.4 $Wm^{-1}K^{-1}$ at 523K.

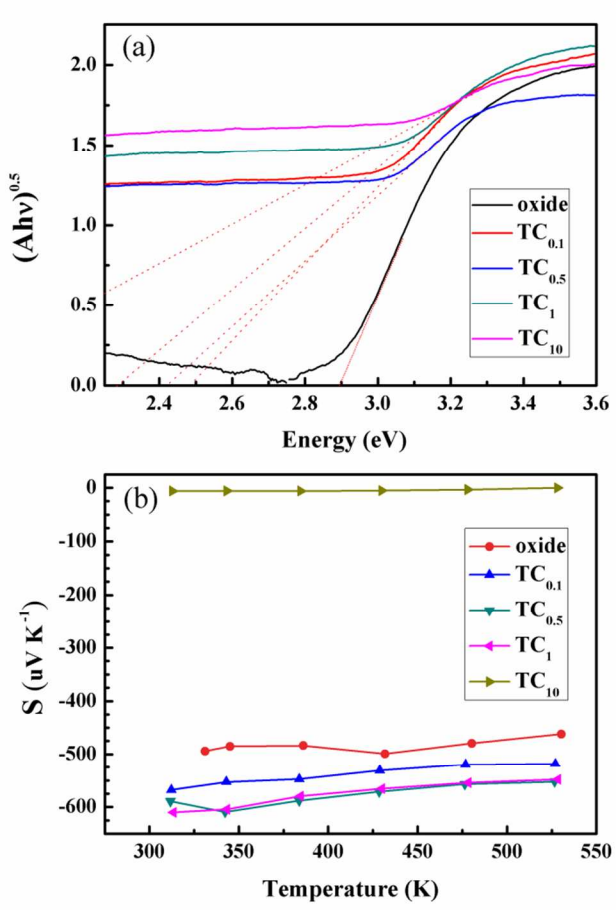

Fig. 5. The uv-vis spectra (a) and S profiles (b) of oxide and composites.

Fig. 6(b) plots σS^2 against f_{CNT} at 300-523K. Again, improvement is evident by a large gap between pure oxide and $TC_{0.1\sim1}$; the former lies on 10^{-7} $Wm^{-1}K^{-2}$ and 10^{-5} $Wm^{-1}K^{-2}$ for the latter. ZT profiles display a similar trend and gap also reaches two orders of magnitude (Fig. 6(c)). It is worth mentioning that ZT improvements here may not be as large as reported data whereas simultaneous increase in σ/k and S is novel and has not been previously observed. Table 2 compares $TC_{0.1}$ with recent reports on single-walled CNTs (SWCNTs)- and graphene-based composites: the negative sign and numbers in brackets indicate negative enhancement and increase with respect to initials. First, addition of CNTs and/or graphenes into TEP matrix results in reduced k, supporting enhanced scattering at interfaces. Second, ZT in MWCNTs/WS_2 and graphene/PbTe systems is promoted at the expense of S. Third, SWCNTs/Bi_2Te_3 shows improved S and reduced σ, thus giving a finite ZT enhancement. Fourth, $TC_{0.1}$ here shows increased σ/k and S and, ZT is enhanced by 7380%. Questions however remain as to why S increases at low f_{CNT}. According to the Ioffe's approximation, S also varies with m^* and is therefore expected to change upon doping. Table 3 lists m_h^*/m_o and m_e^*/m_o along crystallographic planes of [100], [010] and [001] where m_e^*, m_h^* and m_o are masses of electron, hole carriers and free electrons. Note that the m_h^*/m_o and m_e^*/m_o along [001] plane may be ignored because σ is mainly contributed by carriers that have a lower m^* and move along electric field. Calculation shows increase by 61% (m_e^*/m_o) and 27% (m_h^*/m_o) along [100] plane, supporting doping modified carrier mobility. The $m_e^*/m_o > m_h^*/m_o$ also takes place at [010] plane and increase is measured to be 62% and 25%.

Table 2. TEP parameters of $TC_{0.1}$ in comparison with reported data at room T

TEP / Samples	σ (Scm^{-1})	S (μVK^{-1})	σS^2 ($\mu Wm^{-1}K^{-2}$)	k ($Wm^{-1}K^{-1}$)	ZT
SWCNTs$_{(0.5w.t\%)}$ /Bi_2Te_3 [23]	200 (-50%)	231.2 (65.1%)	1069 (36.4%)	1.20 (-13%)	0.27 (56.81%)
MWCNTs$_{(0.75w.t\%)}$ /WS_2 [8]	3 (12300%)	510 (-22%)	68.4 (7330%)	3.3 (-43.1%)	6.21×10^{-3} (12783%)
Graphene$_{(3w.t\%)}$ /PbTe [24]	234 (1021%)	200 (-46.67%)	936 (289%)	0.93 (-51.8%)	0.3 (602%)
Graphene$_{(2.5w.t\%)}$ /$CuInTe_2$ [25]	30 (10.42%)	240 (-5.88%)	173 (-2.26%)	3.825 (-1.29%)	1.36×10^{-2} (-1.02%)
$TC_{0.1}$	0.71 (4249%)	552.8 (14%)	21.5 (5553%)	2.43 (-24.8%)	3.04×10^{-3} (7380%)

The numbers in brackets denote increase % with respect to initials and negative sign indicates a negative enhancement.

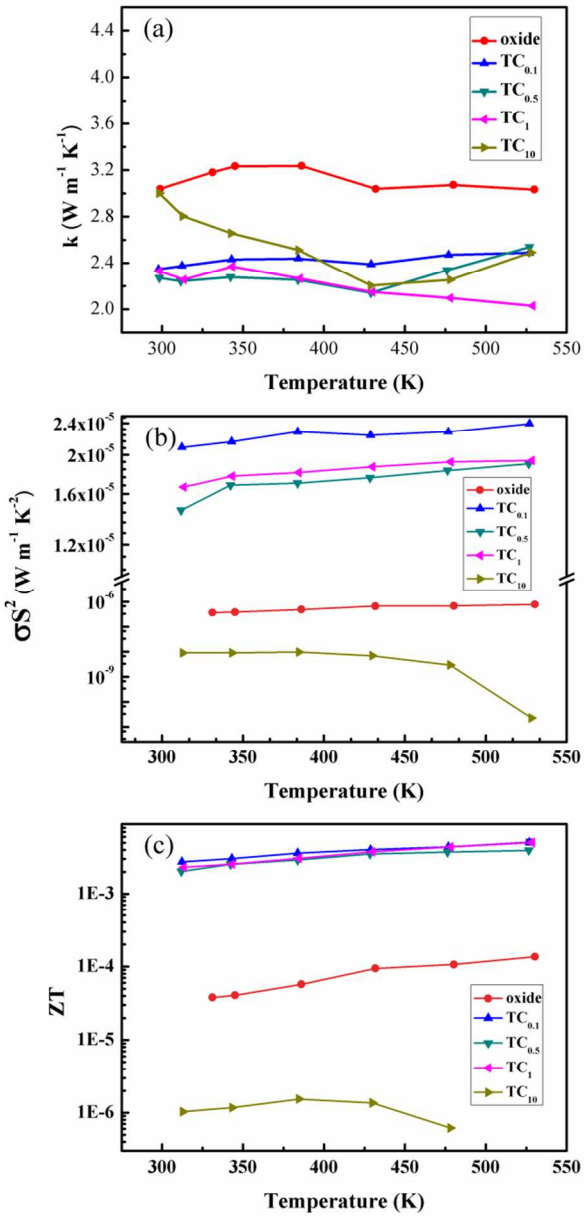

Fig. 6. The k (a), σS^2 (b) and ZT profiles (c) of oxide and doped oxides.

Table 3. The m^* obtained from *ab-initio* calculation

planes	[100]		[010]		[001]	
samples	m_e^*/m_o	m_h^*/m_o	m_e^*/m_o	m_h^*/m_o	m_e^*/m_o	m_h^*/m_o
TiO_2	0.77	3.06	0.77	3.06	8.67	4.36
C-TiO_2	1.24	3.89	1.25	3.84	2.99	6.84

The m_o is the free electron mass and m_e^* and m_h^* represent m^* of electrons and holes in minimum of LUMO and maximum of HOMO.

Conclusions

$CNTs/TiO_2$ composites made by SPS technique exhibit increased σ/k and S and the underlying mechanism involves lengthening of mean free path and m^* change upon tube addition. The weak tube-oxide coupling induces interfacial scattering and results in reduced k. S is negative at low f_{CNT} and increases from $TC_{0.1}$ to TC_1. TC_{10} is governed by p-type CNTs and S decreases toward positive regime. Tube addition creates doped state below LUMO and m_e^*/m_o increases by 61-62% along (100) and (010) planes, accounting for increased S.

Acknowledgements

Yao-Cheng Lai acknowledges the scholarship of "Summer Program, 2013" from the Interchange Association in Japan and Ministry of Science and Technology (MOST) of Taiwan for the financial support (MOST-103-2112-M-007-009-MY2).

Notes and references

[a] Department of Materials Science and Engineering, National Tsing Hua University, Hsinchu 30013, Taiwan

[b] Faculty of Engineering, Iwate University, 4-3-5 Ueda, Morioka 020-8551, Japan

References

1. H. Wang, Y. Pei, A. D. LaLonde and G. J. Snyder, *Advanced Materials*, 2011, **23**, 1366-1370.
2. W. Xie, J. He, H. J. Kang, X. Tang, S. Zhu, M. Laver, S. Wang, J. R. D. Copley, C. M. Brown, Q. Zhang and T. M. Tritt, *Nano Lett.*, 2010, **10**, 3283-3289.
3. Y. Zhang, M. L. Snedaker, C. S. Birkel, S. Mubeen, X. Ji, Y. Shi, D. Liu, X. Liu, M. Moskovits and G. D. Stucky, *Nano Lett.*, 2012, **12**, 1075-1080.
4. M. Ohtaki, D. Ogura, K. Eguchi and H. Arai, *J. Mater. Chem.*, 1994, **4**, 653-656.
5. H. Lu, P. G. Burke, A. C. Gossard, G. Zeng, A. T. Ramu, J.-H. Bahk and J. E. Bowers, *Advanced Materials*, 2011, **23**, 2377-2383.
6. M. Ohtaki, H. Koga, T. Tokunaga, K. Eguchi and H. Arai, *J. Solid State Chem.*, 1995, **120**, 105-111.
7. M. H. Lee, J. S. Rhyee, M. Vaseem, Y. B. Hahn, S. D. Park, H. J. Kim, S. J. Kim, H. J. Lee and C. Kim, *Appl. Phys. Lett.*, 2013, **102**, 223901.
8. D. Suh, D. Lee, C. Kang, I.-J. Shon, W. Kim and S. Baik, *J. Mater. Chem.*, 2012, **22**, 21376-21381.
9. L. Xiong, J. Li and Y. Yu, *Energies*, 2009, **2**, 1009-1030.
10. Q. He, Q. Hao, G. Chen, B. Poudel, X. Wang, D. Wang and Z. Ren, *Appl. Phys. Lett.*, 2007, **91**, 052505.
11. M. Backhaus-Ricoult, J. Rustad, D. Vargheese, I. Dutta and K. Work, *J. Electron Mater.*, 2012, **41**, 1636-1647.
12. W. Wunderlich, H. Ohta and K. Koumoto, *Physica B: Condensed Matter*, 2009, **404**, 2202-2212.
13. C.-C. Li, C.-L. Lu, Y.-T. Lin, B.-Y. Wei and W.-K. Hsu, *Physical Chemistry Chemical Physics*, 2009, **11**, 6034-6037.
14. H.-C. Wen, C.-I. Hung, H.-J. Tsai, C.-K. Lu, Y.-C. Lai and W.-K. Hsu, *J. Mater. Chem.*, 2012, **22**, 13747-13750.
15. Y. Lv, J. Willkomm, A. Steiner, L. Gan, E. Reisner and D. S. Wright, *Chemical Science*, 2012, **3**, 2470-2473.
16. J.-G. Li, T. Ishigaki and X. Sun, *The Journal of Physical Chemistry C*, 2007, **111**, 4969-4976.
17. C. R. Aita, *Appl. Phys. Lett.*, 2007, **90**, 213112.

18. G. Liu, X. Yan, Z. Chen, X. Wang, L. Wang, G. Q. Lu and H.-M. Cheng, *J. Mater. Chem.*, 2009, **19**, 6590-6596.
19. X.-X. Zou, G.-D. Li, J. Zhao, J. Su, X. Wei, K.-X. Wang, Y.-N. Wang and J.-S. Chen, *International Journal of Photoenergy*, 2012, **2012**.
20. S.-Y. Lu, C.-W. Tang, Y.-H. Lin, H.-F. Kuo, Y.-C. Lai, M.-Y. Tsai, H. Ouyang and W.-K. Hsu, *Appl. Phys. Lett.*, 2010, **96**, 231915.
21. M. S. Dresselhaus, G. Dresselhaus, J. C. Charlier and E. Hernández, *Philosophical Transactions of the Royal Society of London. Series A: Mathematical, Physical and Engineering Sciences*, 2004, **362**, 2065-2098.
22. J. Hone, M. Whitney, C. Piskoti, A. Zettl, *Phys. Rev. B*, 1999, **59**, 2514-2516.
23. Y. Zhang, X. L. Wang, W. K. Yeoh, R. K. Zheng and C. Zhang, *Appl. Phys. Lett.*, 2012, **101**, 031909.
24. J. Dong, W. Liu, H. Li, X. Su, X. Tang and C. Uher, *Journal of Materials Chemistry A*, 2013, **1**, 12503-12511.
25. H. Chen, C. Yang, H. Liu, G. Zhang, D. Wan and F. Huang, *CrystEngComm*, 2013, **15**, 6648-6651.